Shell effects in quasifission in reactions forming the ^{226}Th compound nucleus

H. Lee, P. McGlynn, and C. Simenel
Department of Fundamental and Theoretical Physics and Department of Nuclear Physics and Accelerator Applications, Research School of Physics, The Australian National University, Canberra ACT 2601, Australia

(Received 4 March 2024; revised 23 May 2024; accepted 24 July 2024; published 12 August 2024)

Background: Quasifission reactions occur in fully damped heavy-ion collisions without the formation of an equilibrated compound nucleus, leading to the formation of fragments with properties similar to those in fission reactions. In particular, similar shell effects are expected to affect fragment formation in both fission and quasifission. Experimentally, the role of shell effects in quasifission is still debated, and further theoretical predictions are needed.
Purpose: We aim to investigate quasifission dynamics in different reactions forming the same compound nucleus and to search for possible signatures of shell effects in fragment formation.
Methods: ^{50}Ca + ^{176}Yb and ^{96}Zr + ^{130}Sn quasifission reactions are simulated with the time-dependent Hartree-Fock code SKY3D near the Coulomb barrier. Evolutions of the quadrupole (Q_{20}) and octupole (Q_{30}) moments are interpreted in terms of features of the potential energy surface (PES) of the ^{226}Th compound nucleus.
Results: Both reactions encounter quasifission. In ^{50}Ca + ^{176}Yb, it only occurs at finite angular momenta. In the more symmetric ^{96}Zr + ^{130}Sn reaction with stronger Coulomb repulsion in the entrance channel, quasifission also occurs in central collisions. In agreement with earlier predictions, ^{50}Ca + ^{176}Yb encounters partial mass equilibration that is stopped when the heavy fragment reaches $Z \approx 54$ protons, as in the asymmetric fission mode of ^{226}Th. Interestingly, ^{96}Zr + ^{130}Sn encounters an "inverse quasifission" (multinucleon transfer increasing the mass asymmetry between the fragments) also leading to fragments similar to those in asymmetric fission. In both systems, quasifission trajectories in the (Q_{20}-Q_{30}) plane are found close to the asymmetric fission valley of the ^{226}Th PES.
Conclusions: The observation of an inverse quasifission that goes against expectations from a simple liquid drop picture suggests that shell effects have an influence in quasifission. In addition, the similarity between fragments formed in asymmetric fission and quasifission supports the idea that the same shell effects are at play in both mechanisms. In particular, these were recently attributed to octupole deformed shell effects in $Z = 52$–56 fragments. Interpreting quasifission dynamics with PESs used in fission is naturally limited by the fact that these PESs are usually computed with axial symmetry, no angular momentum, and no excitation energy, thus motivating future developments of PESs for quasifission.

DOI: 10.1103/PhysRevC.110.024606

I. INTRODUCTION

Nuclear fission is one of the most complex nuclear processes, thus challenging theoretical many-body modeling [1,2]. In particular, accounting for quantum shell effects in the fissioning system [3–6] as well as in the fragments [6–11] is necessary to explain fission properties such as fragment mass asymmetries observed in experiments [12–18]. Shell effects may also influence the role of dissipation in fission as well as fission time [19].

Shell effects are largely responsible for the topography of potential energy surfaces (PESs) that represent the minimum energy of the system under a set of constraints on its shape, such as quadrupole and octupole moments that are traditionally used to constrain the elongation and asymmetry of the system. In particular, shell effects are able to induce fission valleys driving the system towards asymmetric fission. In fact, shell correction energy [20,21] and single-particle level density near the Fermi level [6] show that several shell effects are at play until scission. Then, the final asymmetry is influenced by shell effects in the prefragments, such as octupole deformed shell effects in the heavy fragment of actinide fission [10].

Shell effects are also expected to play a role in quasifission reactions. The latter occur in fully damped heavy-ion collisions with mass transfer between the fragments, usually producing outgoing fragments that are more symmetric than in the entrance channel [22] (see [23] for a recent review on experimental studies of quasifission). Typical contact times between the fragments in quasifission are of the order of few 10^{-20} s [22,24], i.e., similar to mass equilibration timescale but much slower than other equilibration and dissipation processes [25,26]. Although similar fragments can be produced in quasifission and in fusion followed by fission, there is no formation of an equilibrated compound nucleus in quasifission, and its outgoing fragments could keep a "memory" of the entrance channel. In fact, quasifission is the main mechanism that hinders the formation of superheavy compound nuclei in fusion reactions.

Mass equilibration is expected to stop when shell effects are present in the fragments that prevent further transfer of

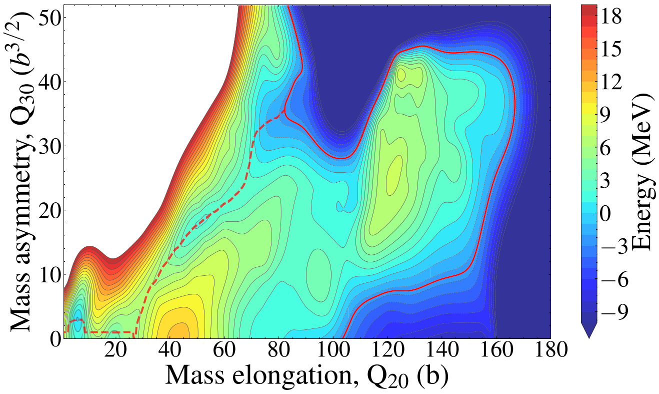

FIG. 1. PES of ^{226}Th obtained using SKYAX with quadrupole and octupole steps $\Delta q_{20} = 1.44$ b and $\Delta q_{30} = 1$ b$^{3/2}$, respectively. The dashed line shows the minimum energy fission path. The solid red line is the scission line.

nucleons. For instance, the formation of fragments in the vicinity of ^{208}Pb in reactions with actinide targets is expected to be favored by its spherical shell effects. Experimental signatures have been discussed in the literature [27–32]. However, it was recently proposed that sequential fission of the target-like fragment could be responsible for the peak at $A \approx 208$ nucleons obtained after rejecting events with three nuclei in the exit channel [33]. Reactions with targets below lead should be free of sequential fission and thus avoid this difficulty. In addition, reactions forming actinide compound nuclei can be used to compare quasifission products with fission modes that are usually known in this region. Nevertheless, even for such lighter systems the influence of shell effects in quasifission is debated, with some experiments finding that "shell effects are clearly seen" [34], while others only conclude "weak evidences" [35].

Several theoretical approaches have been used to investigate quasifission mechanisms, including the dinuclear system model [36–38], models based on the Langevin equation [39–41], molecular dynamics [42–45], the Boltzmann-Uehling-Uhlenbeck model [46], and the time-dependent Hartree-Fock (TDHF) theory and its extensions [30,31,47–57] (see [58–62] for reviews on TDHF).

Recent TDHF simulations of quasifission in ^{50}Ca + ^{176}Yb collisions predicted that the mass equilibration process stops when the heavy fragment reaches $Z \approx 54$ protons [55]. The corresponding mass and charge asymmetries as well as the total kinetic energy (TKE) of the fragments were shown to match those of the fragments produced in the asymmetric fission mode of the ^{226}Th compound nucleus. These observations support the fact that similar shell effects affect both fission and quasifission. The reason for choosing this system was that ^{226}Th exhibits both symmetric and asymmetric fission modes. However, the symmetric mode was not observed in ^{50}Ca + ^{176}Yb quasifission, which led to the conclusion that not all fission modes are expected to be necessarily produced in quasifission. Several systems leading to the same ^{294}Og compound nucleus were also studied with TDHF in a more recent work [57]. It was shown that at least some quasifission reactions could be interpreted in terms of the topography of the PES despite the simplifications used to compute the latter (no excitation energy, zero angular momentum, and axial symmetry). A similar approach is adopted in the present work, where the topography of the ^{226}Th PES is used to interpret quasifission dynamics in ^{50}Ca + ^{176}Yb and ^{96}Zr + ^{130}Sn reactions. The second reaction, being more symmetric than the asymmetric fission mode of ^{226}Th, was chosen with the anticipation that more symmetric quasifission fragments could be produced if they were driven by the symmetric fission valley.

The details of PES and TDHF calculations are described in Sec. II. The quasifission simulations with TDHF are analyzed in Sec. III. The quasifission dynamics is interpreted in terms of the ^{226}Th PES in Sec. IV. Conclusions are drawn in Sec. V. Tables summarizing TDHF results are provided in the Appendix.

II. METHOD

A. PES and fission modes

The PES is a landscape of nuclear potential energies associated with mean-field states of various nuclear shapes. It is commonly computed in terms of multipole moments. In particular the quadrupole moment

$$Q_{20} = \sqrt{\frac{5}{16\pi}} \int d^3r \rho(\mathbf{r})(2z^2 - x^2 - y^2), \tag{1}$$

provides a proxy for the elongation of the system, while the octupole moment

$$Q_{30} = \sqrt{\frac{7}{16\pi}} \int d^3r \rho(\mathbf{r})[2z^3 - 3z(x^2 + y^2)] \tag{2}$$

is a measure of its asymmetry.

Here, the PES is computed from the constrained Hartree-Fock (HF) theory with axial symmetry on nuclear shapes. The states used to build the PES have no internal excitation and their average angular momentum is zero. The PES of ^{226}Th shown in Fig. 1 was calculated with constraints on Q_{20} and Q_{30} with the SLy4d Skyrme functional [63] and BCS pairing interaction with density dependent delta interaction using the SKYAX code [64]. The minimum energy fission path from the ground-state to scission corresponds to the dashed line in Fig. 1. This is the path taken by increasing Q_{20} and choosing Q_{30} to give the minimal energy. The valley which the dashed line follows corresponds to the asymmetric fission valley, whereas the symmetric fission valley leads to scission configurations at $Q_{30} \simeq 0$. The scission line is determined as a set of points in the PES where the neck density falls below $\rho = 0.08$ fm^{-3}.

B. TDHF simulations

The TDHF mean-field theory can be obtained from a variational principle on Dirac action, leading to an equation on the one-body density matrix ρ,

$$i\hbar \frac{d\rho}{dt} = [h[\rho], \rho], \tag{3}$$

where $h[\rho]$ is the Hartree-Fock single-particle Hamiltonian. Here, it is obtained from a Skyrme energy density functional

$E[\rho]$ according to $h[\rho]_{\alpha\beta} = \frac{\delta E[\rho]}{\delta \rho_{\beta\alpha}}$. The HF Hamiltonian is self-consistent as it depends on the one-body density matrix ρ of the system.

The ground states of the collision partners are first obtained from a static mean-field calculation on a Cartesian grid of $28 \times 28 \times 28$ fm^3 with mesh size $\Delta x = 1$ fm. As in PES calculations, the SLy4*d* Skyrme functional [63] was used with the same pairing functional to account for pairing correlations at the BCS level. The resulting ground-state wave functions of collision partners are then placed in a larger Cartesian grid with the same mesh size, with an initial distance of 56 fm between the centers of mass. The collision axis between the fragments was aligned with the z axis of the simulation, with the midpoint between the centers of mass of two fragments placed at the origin. Shape coexistence is expected in ^{96}Zr with $\beta_2 \simeq 0.13$ prolate ($\beta_2 \simeq -0.14$ oblate) energy minimum only 0.25 MeV (0.13 MeV) below the spherical configuration. It was then constrained to be spherical to probe the average behavior between prolate and oblate deformations. Furthermore, the spherical ^{96}Zr was time evolved alone in a simulation box to ensure that fluctuations in shape would be minimal over the timescale of the collision. Negligible changes in the quadrupole and octupole moments were found during the time evolution, indicating stability of the spherical mean-field configuration. The ^{176}Yb nucleus is found to have a significant prolate deformation, so, to consider effects of orientation of the target nucleus with respect to the collision axis, the ^{176}Yb nucleus was prepared in two configurations in a grid, rotated by $\frac{\pi}{2}$ radians. For noncentral collisions of ^{50}Ca + ^{176}Yb, the side and tip orientations refer to the initial orientation of ^{176}Yb with respect to the z axis of the simulation.

A Galilean boost is applied on each nucleus according to the required center-of-mass energy $E_{\text{c.m.}}$ and the initial orbital angular momentum L, assuming that prior to this initial condition, the nuclei followed a Rutherford trajectory. The TDHF equation is then solved iteratively in time with a time step $\Delta t = 0.2$ fm/c. The single particle occupation numbers are kept constant in the time evolution according to the frozen occupation approximation (FOA). The FOA allows one to account for static pairing correlations in the initial state, thus providing reasonable deformation of the collision partners. However, it neglects dissipative effects from pairing dynamics as well as effects coming from the difference between gauge angles of collision partners [65–67]. Though it is beyond the scope of this work, it would be interesting to investigate the effect of pairing dynamics on quasifission in the future.

The grid size of the TDHF simulations was set to be $28 \times 28 \times 84$ fm^3 for central collisions and $84 \times 28 \times 84$ fm^3 for noncentral collisions. The simulations were stopped when the system reseparated or when the contact time (defined in Sec. III A 1) exceeded 35 zs. Both static initial conditions and dynamical evolutions are computed with the SKY3D solver [68,69]. The central (noncentral) collisions were run for up to 6 (16) days on eight CPU cores per system. Multiple systems were simulated in parallel on the Australian National Computational Infrastructure's (NCI) Gadi supercomputer.

To search for quasifission, central collisions between pairs of nuclei at energies ranging from $0.9V_B$ to $1.3V_B$ were simulated in 20 equal steps in energy, where V_B is the Coulomb barrier of the system. A finer energy search was run until the fusion threshold could be determined within 0.1 MeV. The barriers were determined according to Świątecki *et al.* [70], and found to be $V_B = 151.8$ MeV and 215.4 MeV for ^{50}Ca + ^{176}Yb and ^{96}Zr + ^{130}Sn, respectively. Noncentral collisions were simulated at fixed energies of 10% above their Coulomb barriers (167 and 237 MeV, respectively) to investigate the effect of angular momentum. The results are summarized in the Appendix.

III. TDHF RESULTS

A. Quasifission properties

1. Contact times

TDHF simulations of heavy-ion collisions do not enforce quasifission to occur, so simulation outcomes that have led to quasifission must be searched for. Characteristics of quasifission include full damping of kinetic energy of the collision partners, significant mass transfer, and contact times exceeding few zeptoseconds. In the following, contact times are used to define criteria for characterisation of the main reaction mechanisms. Here, two nuclei are considered to be in contact when the neck density exceeds 0.08 fm^{-3}, i.e., half of the nuclear saturation density.

The timescale for kinetic energy dissipation being of the order of 2 zs [55], we consider that reactions with contact times $\tau < 2$ zs are not fully damped and are thus not associated with quasifission. Such reactions are generically called hereafter "quasielastic" scattering (QS), though they also include deep-inelastic scattering. Systems with contact times greater than 30 zs were usually associated[1] with "fusion," although, strictly speaking, these include potential slow quasifission as well.

^{50}Ca + ^{176}Yb central collisions are characterised by a rapid transition from quasielastic scattering to fusion (see $L = 0$ entries in Tables II and III in the Appendix). For each orientation, only one reseparation occurred at $\tau > 2$ zs contact time: $\tau = 2.75$ zs at $E_{\text{c.m.}} = 145.6$ MeV (tip) and $\tau = 2.09$ zs at $E_{\text{c.m.}} = 156.8$ MeV (side). In each case, less than one nucleon is transferred in average. The relatively short contact times and small mass transfer indicate that these reactions could still be considered as QS. With only 0.1 MeV increase in energy, these systems fuse with contact times exceeding 35 zs. We conclude that no quasifission occurs in TDHF simulations of ^{50}Ca + ^{176}Yb central collisions. This is in contrast with heavier systems [47,57].

The simulation results for ^{50}Ca + ^{176}Yb collisions with the side orientation at various angular momenta and center-of-mass energies are presented in Fig. 2(a). Interestingly, quasifission is observed at finite orbital angular momentum in the transition between fusion and QS. A similar behavior was also seen with the tip oriented collisions in Fig. 2(b).

In contrast with ^{50}Ca + ^{176}Yb, quasifission occurs in ^{96}Zr + ^{130}Sn central collisions as indicated by contact times

[1] In some cases where the system's elongation was increasing at $\tau \simeq 35$ zs, simulations were run for a longer time.

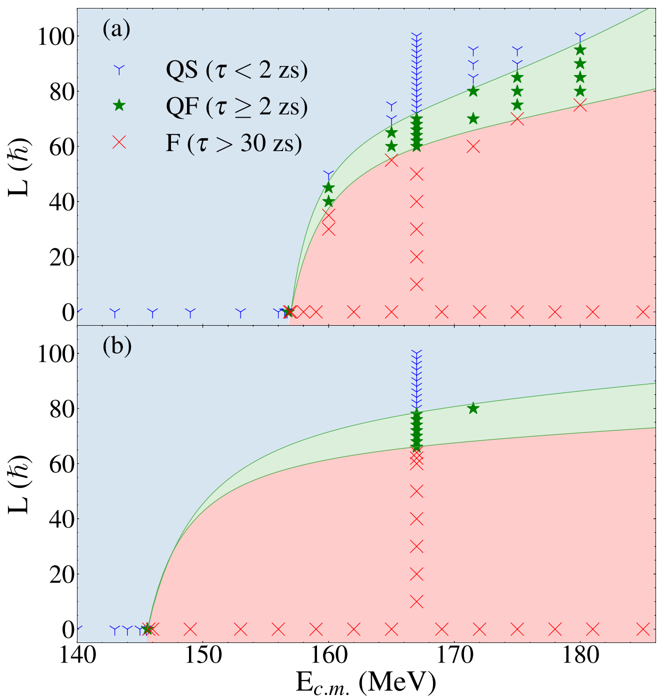

FIG. 2. Simulated results for side-oriented (a) and tip-oriented (b) ^{50}Ca + ^{176}Yb. Each point corresponds to a TDHF simulation. The blue, green, and red shaded regions correspond to regions assigned to "quasielastic" scattering (QS), "quasifission" (QF), and "fusion" (F), respectively. The region boundaries are only approximate guidelines, obtained by fitting a quadratic polynomial in inverse energy.

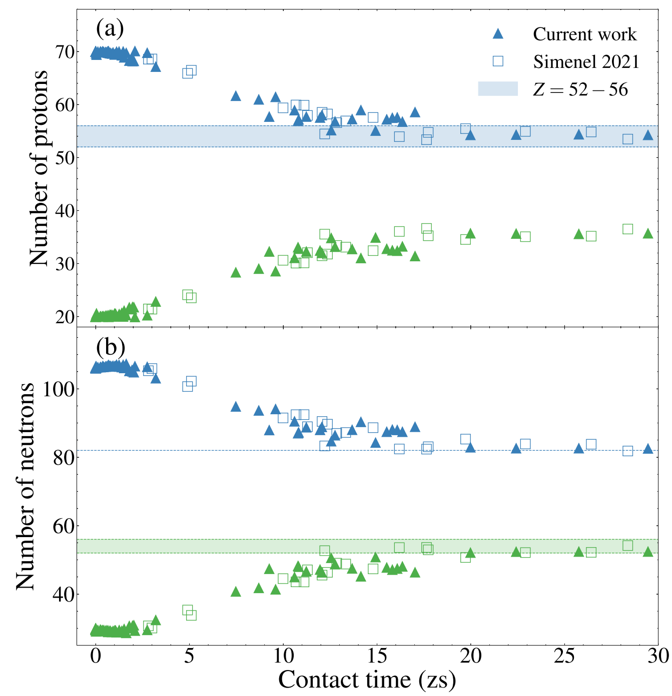

FIG. 4. Numbers of (a) protons and (b) neutrons in the outgoing fragments of ^{176}Yb + ^{50}Ca collisions against contact time, for both side and tip orientations. The blue and the green symbols correspond to the heavy and light fragments, respectively. Present results are shown as triangles while those of Ref. [55] (Simenel 2021) are shown as squares. The shaded regions at (a) $Z = 52$–56 and (b) $N = 52$–56 indicate expected octupole deformed shell effects. The line in (b) indicates the spherical shell effect at $N = 82$.

exceeding 2 zs between $E_{\text{c.m.}} \approx 221$ MeV and $E_{\text{c.m.}} \approx 232$ MeV as shown in Fig. 3. These contact times keep increasing in central collisions up to $\tau \simeq 9$ zs at $E_{\text{c.m.}} \approx 231$ MeV. These energies are above the Coulomb barrier $V_B = 215.4$ MeV for this system, indicating a fusion hindrance mechanism. However, no reseparation with contact times longer than 10 zs was observed in this system, even in noncentral collisions.

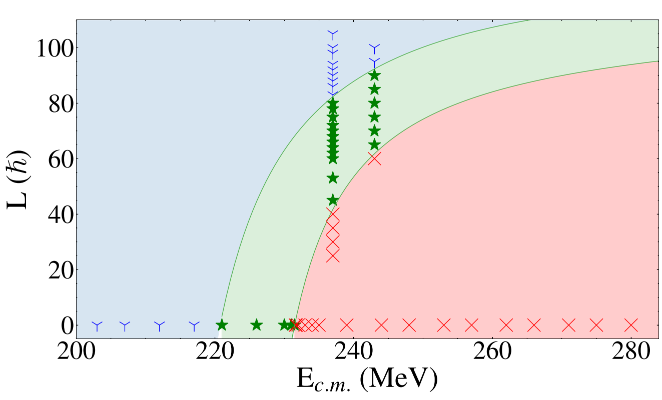

FIG. 3. Simulated results for ^{96}Zr + ^{130}Sn. Each point corresponds to a TDHF simulation. The blue, green, and red shaded regions correspond to regions assigned to "quasielastic scattering" (QS), "quasifission" (QF), and "fusion" (F), respectively. The region boundaries are only approximate guidelines, obtained by fitting a quadratic polynomial in inverse energy.

2. *Mass transfer*

Figure 4 shows the evolution of the number of protons in the fragments with contact time for both side and tip orientations of ^{50}Ca + ^{176}Yb collisions. The results agree well with those of Ref. [55] that were obtained with the TDHF3D code [63]. An increase in the mass transfer is observed with increase in the contact time. However, this mass equilibration process stops for contact times greater than ≈13 zs, where the numbers of protons (neutrons) converge to $Z_L \approx 36$ ($N_L \approx 52$) and $Z_H \approx 54$ ($N_H \approx 82$) in the light and heavy fragments, respectively, as in ^{226}Th asymmetric fission. This could be attributed to several shell effects in the fragments, including octupole deformed shell effects at $Z = 52, 56$ [55] that were proposed to explain the final asymmetry in fission of actinides [10].

The numbers of protons and neutrons in the outgoing fragments produced in ^{96}Zr + ^{130}Sn collisions are plotted in Figs. 5(a) and 5(b), respectively, as a function of contact time. While the numbers of neutrons in the fragments remain close to those of the collision partners, some protons are transferred from ^{96}Zr to ^{130}Sn, moving the latter away from magicity associated with spherical shell gap at $Z = 50$. This transfer occurs within ≈2 zs, a timescale characteristic to

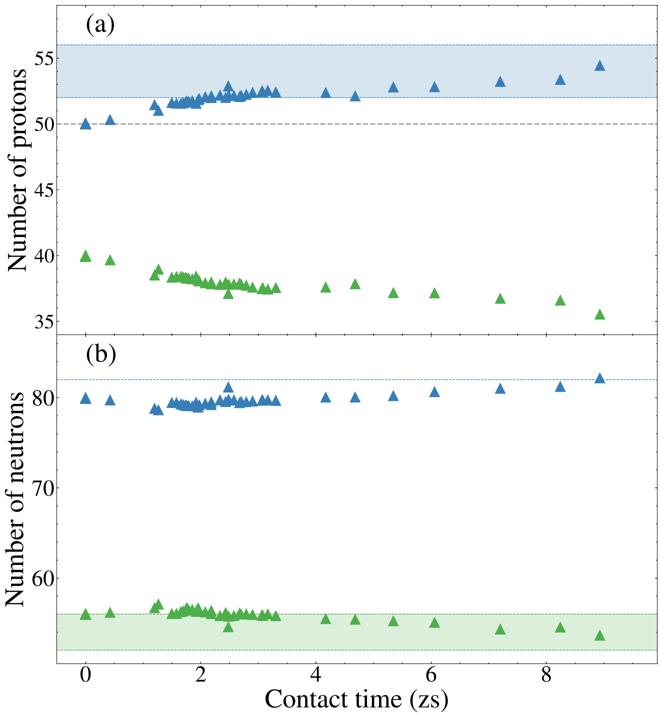

FIG. 5. Numbers of (a) protons and (b) neutrons in the outgoing fragments of $^{96}Zr + ^{130}Sn$ collisions against contact time. The blue and the green symbols correspond to the heavy and light fragments, respectively. The shaded regions at $Z, N = 52$–56 indicate expected octupole deformed shell effects. The lines at $Z = 50$ and $N = 82$ indicate nuclear magic numbers.

neutron-to-proton equilibration [26,71,72]. Indeed, the collision partners have $N/Z = 1.4$ (^{96}Zr) and 1.6 (^{130}Sn), while the fragments exiting the reaction after $\tau \approx 2$ zs contact time have $N/Z \approx 1.5$. The net effect is a larger mass asymmetry in the exit channel than in the entrance one. This asymmetry is slightly increased for longer contact times. This unusual drift away from mass symmetry is referred to as "inverse quasifission." Inverse quasifission was also observed in other systems [73–75] and attributed to orientation or shell effects. As a result, the outgoing fragments formed in $^{96}Zr + ^{130}Sn$ are similar to those produced both in $^{176}Yb + ^{50}Ca$ collisions and in ^{226}Th asymmetric fission, indicating, once again, a possible influence of octupole deformed shell effects in the fragments fixing their final asymmetry.

3. Total kinetic energy

Figure 6 shows the TKE of the outgoing fragments as a function of the mass ratio $M_R = A_{\text{frag.}}/A_{\text{tot.}}$ where $A_{\text{frag.}}$ is the fragment mass number and $A_{\text{tot.}} = 226$ is the total one. The quasifission events have TKE close to Viola systematics [76,77], confirming that these are fully damped events. However, the inverse quasifission events occurring in the $^{96}Zr + ^{130}Sn$ reaction have TKE higher than Viola systematics. This could be attributed to the proximity of $Z = 50$ spherical shell gap that is expected to produce more compact fragments. In particular, the $Z = 52$ octupole deformed shell gap is less deformed (thus leading to more compact

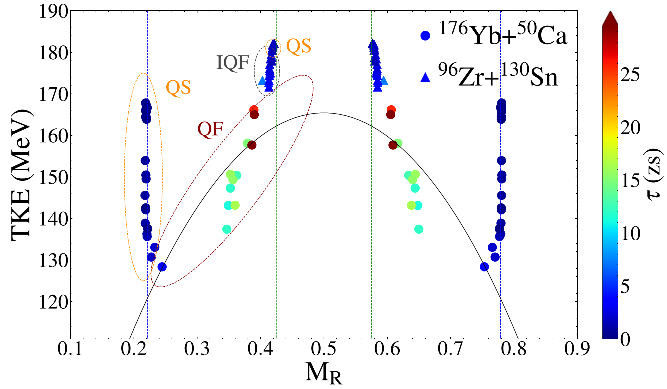

FIG. 6. Total kinetic energy of fragments from collisions of $^{176}Yb + ^{50}Ca$ at $E_{\text{c.m.}} = 167$ MeV and $^{96}Zr + ^{130}Sn$ at $E_{\text{c.m.}} = 237$ MeV as a function of mass ratio M_R. Quasielastic scattering (QS), quasifission (QF), and inverse quasifission (IQF) events are indicated for the light fragments. The blue and green vertical dashed lines show the initial mass ratio for the reacting systems of $^{176}Yb + ^{50}Ca$ and $^{96}Zr + ^{130}Sn$, respectively. The total kinetic energy from Viola systematics [76,77] is shown as the black solid line. The color scale gives the contact time τ of each reaction.

configurations at scission and therefore to higher TKE) than the $Z = 56$ one. Interestingly, the most symmetric events produced in $^{176}Yb + ^{50}Ca$ collisions seem to converge towards the same region of the TKE-M_R plot as the most asymmetric outgoing fragments formed in $^{96}Zr + ^{130}Sn$ inverse quasifission, indicating that the fragments are likely to be produced with similar shapes.

4. Total excitation energy

The total excitation energy (TXE) in the exit channel can be evaluated from $\text{TXE} = Q + E_{\text{c.m.}} - \text{TKE}$, where Q is the Q value for the specific reaction channel. Q values were derived using Ref. [78]. Figure 7 shows a rapid increase of TXE with contact time, followed by a plateau at $\text{TXE} \simeq 70 \pm 10$ MeV at $\tau \gtrsim 5$ zs. The results are obtained for various energies and

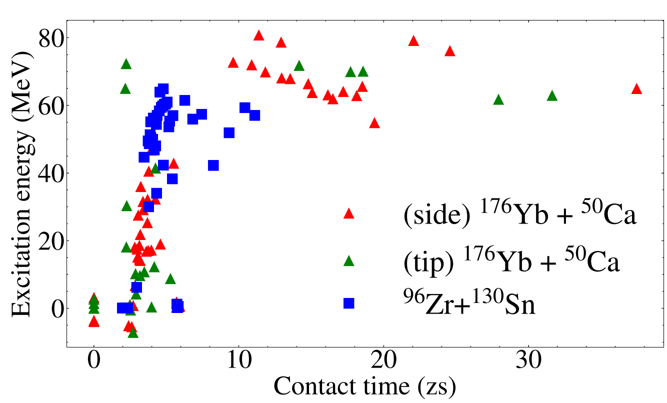

FIG. 7. Total excitation energy (TXE) of the simulated systems as function of contact times. The red and green symbols correspond to collisions between ^{50}Ca and ^{176}Yb in side and tip orientations, respectively. The blue symbols correspond to $^{96}Zr + ^{130}Sn$ collisions.

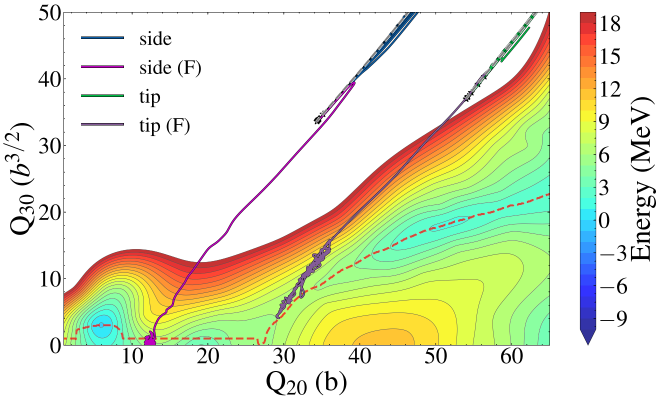

FIG. 8. TDHF trajectories of $^{50}Ca + ^{176}Yb$ central collisions at $E_{c.m.} = 140$–145.7 MeV ($E_{c.m.} = 153$–156.9 MeV) with tip (side) orientation are drawn in the Q_{20}-Q_{30} plane on top of the PES. Trajectories leading to "fusion" are denoted by (F). The entrance channel trajectories are shown by the black dashed lines and the entry (contact) point are represented by stars. The colored solid lines represent trajectories after contact. The orange dashed line shows the minimum energy fission path.

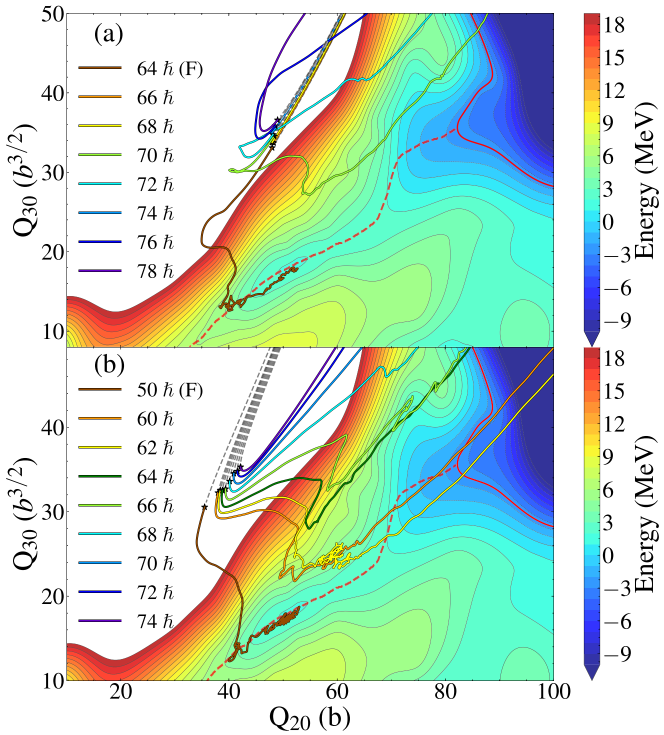

FIG. 9. Same as Fig. 8 for quasifission trajectories of $^{50}Ca + ^{176}Yb$ at $E_{c.m.} = 167$ MeV and various angular momenta for tip (a) and side (b) orientations.

impact parameters, indicating little dependence of quasifission outcome with energy and angular momentum.

This TXE is shared by the outgoing fragments (see Ref. [50] for an evaluation of this repartition in other systems from the density-constrained TDHF method). The resulting excitation energy at scission could, in principle, be large enough to wash out shell effects. It should be noted, however, that the systems are not thermalized at scission and a significant fraction of the excitation energy is expected to be stored into deformation energy and collective modes. Evaluating the repartition between different types of excitation energy is an interesting prospect for future studies.

IV. QUASIFISSION TRAJECTORIES

Let us know compare TDHF trajectories in the Q_{20}-Q_{30} plane with the PES, as in Ref. [57]. This is done in Figs. 8 and 9 for $^{50}Ca + ^{176}Yb$ central and noncentral collisions, respectively, and in Fig. 11 for $^{96}Zr + ^{130}Sn$ central collisions. Each trajectory can be divided into two parts: the entrance channel trajectory where the two colliding nuclei have yet to touch (dashed line) and the following trajectory where the nuclei are in contact (solid line). The entry point where the two nuclei first make contact is represented by a star.

A. $^{50}Ca + ^{176}Yb$

As discussed earlier, $^{50}Ca + ^{176}Yb$ central collisions do not lead to quasifission. The Q_{20}-Q_{30} TDHF trajectories that lead to a reseparation in Fig. 8 then follow closely the entrance channel trajectory, which is compatible with quasielastic scattering. Above the fusion threshold, the system then drifts toward the formation of a more compact system. In particular, the side orientation, which is more compact at the entry point, evolves toward a shape with $Q_{30} \approx 0$ and an elongation comparable to that of the first fission barrier. Note that central collisions with side orientations lead to nonaxial shapes. Thus using features of the axial PES to interpret TDHF trajectories for side orientations should be done with care. Central collisions with the tip orientation, however, should preserve their entrance channel axial symmetry. In this case, the PES is relevant to interpret the TDHF trajectories, assuming that excitation energy does not affect the PES topography. We see in Fig. 8 that the tip orientation leading to fusion evolves toward a shape with elongation and asymmetry compatible with the second barrier (or saddle point). It is interesting to see that both "fusion" trajectories in Fig. 8 lead to configurations close to the minimum energy fission path. The tip orientation, in particular, might also follow this path to scission, leading to a so-called "slow" quasifission.

Figures 9(a) and 9(b) show the TDHF trajectories for $^{50}Ca + ^{176}Yb$ at $E_{c.m.} = 167$ MeV at finite L with the tip and side orientations, respectively. The underlying PES, being computed at $L = 0$ and assuming axial symmetry, provides only a qualitative tool for comparing with TDHF trajectories, which, for noncentral collisions, all break axial symmetry.

Nevertheless, it is interesting to see that the few peripheral collisions that still lead to quasifission do it by following the asymmetric fission valley. Moreover, the trajectories that are associated with "fusion," seem in fact to get trapped into a local minimum along the minimum energy fission path. This could be an indication that some features of the PES remain relevant at finite L and for nonaxial shapes, or that the system evolves towards approximately axial shapes during the reaction.

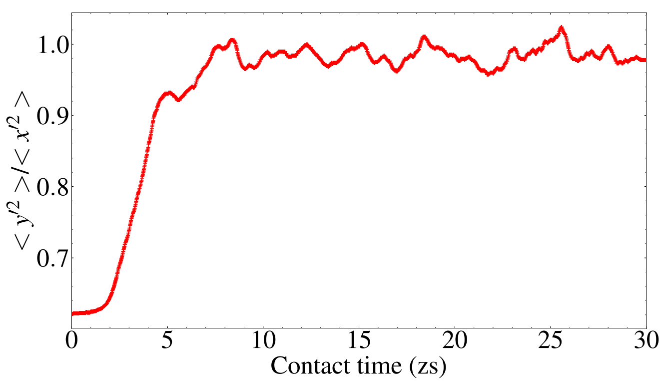

FIG. 10. Time evolution of $\langle y'^2\rangle/\langle x'^2\rangle$ (see text for definition) for ^{50}Ca + ^{176}Yb (side orientation) at $E_{\mathrm{c.m.}} = 167$ MeV and $L = 50\hbar$.

To get a deeper insight into the shape evolution of the system, the principal axis z' was determined from diagonalization of the Cartesian quadrupole tensor. The ^{176}Yb deformation axis is initially in the collision plane (x, z), thus the z' axis also remains in the collision plane (so does, by definition, the x' axis). Thus, for an axially symmetric system, one would expect $\langle x'^2\rangle = \langle y'^2\rangle$. Figure 10 shows the evolution of $\langle y'^2\rangle/\langle x'^2\rangle$ for the ^{50}Ca + ^{176}Yb reaction with the side orientation at $E_{\mathrm{c.m.}} = 167$ MeV and $L = 50\hbar$ that seems to get "trapped" into a pocket of the PES in Fig. 9(b) (solid brown line). We see that this ratio is initially smaller than 1, indicating a nonaxial shape. However, it rapidly increases and become approximatively constant with $\langle y'^2\rangle/\langle x'^2\rangle \simeq 1$, compatible with a quasiaxial shape. In this case, the comparison between the trajectory and the PES topography is meaningful despite the initial nonaxiality. Note that not all systems are guaranteed to evolve towards an axial shape (see, e.g., Ref. [57]). Thus the shape of the system should be studied (e.g., through the ratio $\langle y'^2\rangle/\langle x'^2\rangle$ as in the example of Fig. 10) whenever a comparison with the PES is relevant.

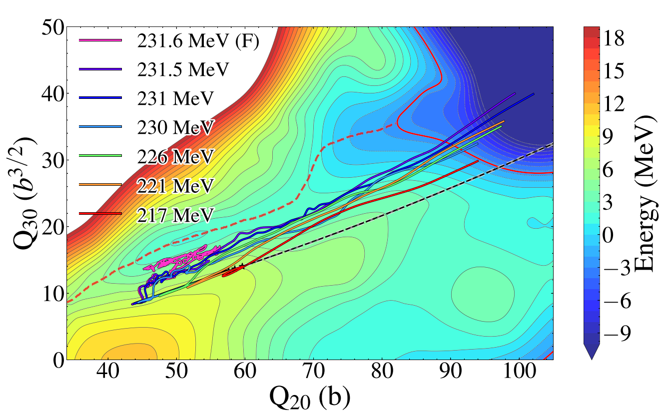

FIG. 11. Same as Fig. 8 for ^{96}Zr + ^{130}Sn central collisions at $E_{\mathrm{c.m.}} = 217$–235 MeV.

TABLE I. Exit channel properties of ^{96}Zr + ^{130}Sn. Energies ($E_{\mathrm{c.m.}}$ and TKE) are in MeV, angular momenta (L) in units of $\hbar$, and contact times (τ) in zeptoseconds (zs). Subscripts H and L refer to heavy and light fragments, respectively.

$E_{\mathrm{c.m.}}$	L	τ	A_H	A_L	Z_H	Z_L	TKE
203	0	0.00	129.99	95.98	50.08	39.92	201.76
207		0.43	130.07	95.87	50.33	39.67	200.81
212		1.27	129.68	96.07	51.02	38.96	177.02
217		1.92	131.04	94.73	51.56	38.43	177.74
221		2.48	134.06	91.71	52.88	37.11	171.91
226		3.16	132.29	93.47	52.54	37.45	172.39
230		6.06	133.49	92.25	52.82	37.17	174.75
231		8.24	134.62	91.17	53.38	36.61	167.63
231.5		8.93	136.64	89.21	54.44	35.55	167.82
231.6		>35					
237	40	>30					
	45	7.20	134.26	91.09	53.22	36.75	173.24
	53	4.68	132.20	93.28	52.13	37.85	172.69
	60	3.30	132.11	93.38	52.42	37.56	171.64
	62	3.08	132.14	93.40	52.43	37.55	173.27
	64	2.90	132.02	93.55	52.39	37.60	174.48
	66	2.79	131.79	93.76	52.24	37.74	175.01
	68	2.70	131.75	93.81	52.16	37.82	175.16
	70	2.58	131.88	93.68	52.15	37.83	175.64
	72	2.48	131.98	93.58	52.17	37.81	176.07
	75	2.33	131.93	93.63	52.18	37.80	177.08
	78	2.18	131.66	93.91	52.13	37.85	178.42
	80	2.08	131.42	94.17	52.06	37.93	179.41
	83	1.97	131.11	94.49	51.91	38.07	180.60
	86	1.85	130.85	94.74	51.75	38.23	181.77
243	60	>30					
	65	5.34	133.02	92.44	52.80	37.18	172.63
	70	4.17	132.44	93.11	52.38	37.60	173.15
	75	3.06	132.26	93.42	52.51	37.48	174.03
	80	2.67	131.52	94.02	52.07	37.91	176.56
	85	2.43	131.58	94.14	52.01	37.98	177.54
	90	2.18	131.23	94.38	52.00	37.99	179.04
	95	1.95	130.78	94.85	51.83	38.16	181.51
	100	1.76	130.85	94.99	51.72	38.28	182.62

B. ^{96}Zr + ^{130}Sn

Figure 11 shows the TDHF trajectories in ^{96}Zr + ^{130}Sn central collisions[2]. After contact, the trajectories follow more asymmetric exit channels leading to inverse quasifission. Axial symmetry should be preserved in these reactions and thus a comparison with the underlying PES is meaningful. Interestingly, the trajectories all seem to "hit" the second barrier, preventing all but the highest energy to fuse. As discussed earlier, proton-to-neutron equilibration may explain the initial increase in asymmetry. However, the presence of the asymmetric fission valley seems to further drive the systems towards inverse quasifission.

[2]Noncentral collisions, not shown in Fig. 11, exhibit a similar behavior. See also Table I in the Appendix.

V. DISCUSSION AND CONCLUSIONS

The influence of shell effects in quasifission was studied with TDHF simulations of $^{50}Ca + ^{176}Yb$ and $^{96}Zr + ^{130}Sn$ reactions. The trajectories in the Q_{20}-Q_{30} plane were compared to the PES of the ^{226}Th compound nucleus. Mass equilibration in the $^{50}Ca + ^{176}Yb$ reaction stops when the system reaches the asymmetric fission valley of ^{226}Th, leading to heavy fragments with $Z \approx 54$ protons. This is an indication that quasifission can be affected by the same shell effects as in fission. In this case, the octupole deformed shell effects at $Z = 52$ and 56 are invoked as a factor impacting the final asymmetry of the system [10].

The exit trajectories of $^{96}Zr + ^{130}Sn$ are found to be more mass asymmetric than the entrance channel ones, contrary to the expectation based on a simple liquid drop model of quasifission which usually drives the system towards fragment mass symmetry. The rapid neutron-to-proton equilibration may explain an initial drive towards asymmetry. Although the TDHF trajectories do not follow closely the bottom of the asymmetric fission fission valley, the latter seem to further drive the systems towards inverse quasifission. No trajectories were found to enter the symmetric fission valley in the ^{226}Th PES for this reaction. As such, the observation of more mass-asymmetric $^{96}Zr + ^{130}Sn$ trajectories, potentially affected by the asymmetric fission valley, further suggests that quasifission is subject to shell effects.

In many situations, the comparison between TDHF trajectories and PES remains qualitative as the PES is computed assuming zero excitation energy, zero angular momentum, and axial symmetry. Each of these assumptions is expected to break down in heavy-ion collisions. It would therefore be interesting to compute PESs without these assumptions in order to investigate their effects on the PES topography, and in particular, on the fission valleys induced by shell effects.

ACKNOWLEDGMENTS

This work has been supported by the Australian Research Council Discovery Project (Project No. DP190100256). Computational resources were provided by the Australian Government through the National Computational Infrastructure (NCI) under the ANU Merit Allocation Scheme, the Adapter scheme, and the National Committee Merit Allocation Scheme. H.L. acknowledges the support of the Australian National University through the Dunbar Physics Honours scholarship. P.M. acknowledges the support of the Australian National University through the Deakin Ph.D. scholarship and the Dean's Merit Scholarship in science.

APPENDIX: TDHF SIMULATION RESULTS

The TDHF simulation results are summarized in Tables I–III.

TABLE II. Same as Table I for $^{50}Ca + ^{176}Yb$(tip).

$E_{c.m.}$	L	τ	A_H	A_L	Z_H	Z_L	TKE
140	0	0.00	176.40	49.58	70.00	20.00	138.94
143		0.38	176.66	49.29	70.02	19.98	138.01
144		0.64	176.69	49.21	69.99	20.00	133.58
145		0.93	176.52	49.39	69.80	20.20	133.46
145.5		1.63	177.01	48.90	69.74	20.26	132.46
145.6		2.75	176.16	49.77	69.75	20.25	136.85
145.7		>35					
167	64	>35					
	66	25.76	137.01	88.01	54.38	35.60	166.16
	68	29.45	136.81	88.13	54.26	35.71	165.00
	70	15.52	144.64	80.54	57.20	32.79	149.36
	72	11.96	145.52	79.62	57.53	32.45	147.30
	74	12.06	146.84	78.34	57.98	32.01	137.42
	76	16.35	144.19	81.30	56.76	33.24	143.18
	78	2.03	173.05	52.66	68.22	21.77	133.05
	80	0.04	175.54	50.13	69.39	20.59	137.51

TABLE III. Same as Table I for $^{50}Ca + ^{176}Yb$(side).

$E_{c.m.}$	L	τ	A_H	A_L	Z_H	Z_L	TKE
153	0	0.00	176.20	49.78	70.01	19.99	151.19
156		0.68	177.02	48.88	70.05	19.95	141.09
156.5		1.11	177.02	48.89	69.96	20.04	138.87
156.6		1.25	176.99	48.92	69.98	20.02	138.75
156.7		1.47	177.00	48.90	69.99	20.01	138.73
156.8		2.09	176.67	49.23	70.07	19.93	137.05
156.9		>35					
160	35	>35					
	40	16.08	145.55	79.86	57.57	32.42	146.50
	45	13.67	145.26	80.23	57.25	32.75	140.83
	50	1.25	176.00	49.94	69.52	20.47	134.72
165	55	>35					
	60	17.03	147.47	77.78	58.57	31.42	148.15
	65	14.14	149.28	76.22	58.95	31.05	139.28
	70	1.03	176.11	49.84	69.52	20.48	135.88
	75	0.77	176.40	49.49	69.75	20.25	144.16
167	50	>35					
	60	14.92	139.35	85.71	55.07	34.91	158.12
	62	35.17	137.61	87.28	54.63	35.35	157.67
	64	12.76	143.22	81.90	56.81	33.18	150.38
	66	15.82	145.56	79.62	57.49	32.50	150.60
	68	11.23	146.47	78.91	57.72	32.27	143.13
	70	3.20	170.22	55.26	67.13	22.84	128.36
	72	1.93	174.04	51.43	68.56	21.40	130.71
	74	1.39	175.61	49.94	69.28	20.69	135.65
171.5	60	>35					
	70	12.56	139.83	85.42	55.16	34.83	159.63
	80	9.59	155.52	69.93	61.44	28.56	135.71
	85	1.52	174.96	50.90	68.88	21.11	133.50
	90	0.76	176.33	49.58	69.66	20.33	144.02
175	75	22.42	136.93	88.05	54.31	35.66	159.79
	80	10.79	143.92	81.31	56.91	33.08	153.15
	85	8.70	154.62	70.83	60.95	29.04	139.61
	90	1.96	173.26	52.55	68.18	21.81	133.75
	95	1.01	175.98	49.87	69.42	20.57	139.86
180	80	19.98	137.16	87.82	54.26	35.71	161.78
	85	10.82	144.43	80.79	57.18	32.80	147.58
	90	9.25	145.65	79.67	57.71	32.28	151.31
	95	7.47	156.48	69.11	61.64	28.35	135.49
	100	1.79	173.47	52.42	68.26	21.74	135.25

[1] M. Bender, R. Bernard, G. Bertsch, S. Chiba, J. J. Dobaczewski, N. Dubray, S. Giuliani, K. Hagino, D. Lacroix, Z. Li, P. Magierski, J. Maruhn, W. Nazarewicz, J. Pei, S. Péru-Desenfants, N. Pillet, J. Randrup, D. Regnier, P.-G. Reinhard, L. M. Robledo *et al.*, Future of nuclear fission theory, J. Phys. G: Nucl. Part. Phys. **47**, 113002 (2020).

[2] N. Schunck and D. Regnier, Theory of nuclear fission, Prog. Part. Nucl. Phys. **125**, 103963 (2022).

[3] C. Gustafsson, P. Möller, and S. G. Nilsson, The microscopic mechanism behind the fission barrier asymmetry, Phys. Lett. B **34**, 349 (1971).

[4] T. Ichikawa and P. Möller, The microscopic mechanism behind the fission-barrier asymmetry (II): The rare-earth region $50 < Z < 82$ and $82 < N < 126$, Phys. Lett. B **789**, 679 (2019).

[5] S. Ćwiok, W. Nazarewicz, J. Saladin, W. Płóciennik, and A. Johnson, Hyperdeformations and clustering in the actinide nuclei, Phys. Lett. B **322**, 304 (1994).

[6] R. N. Bernard, C. Simenel, and G. Blanchon, Hartree-fock-bogoliubov study of quantum shell effects on the path to fission in ^{180}Hg, ^{236}U and ^{256}Fm, Eur. Phys. J. A **59**, 51 (2023).

[7] M. G. Mayer, On closed shells in nuclei, Phys. Rev. **74**, 235 (1948).

[8] L. Meitner, Fission and nuclear shell model, Nature (London) **165**, 561 (1950).

[9] B. D. Wilkins, E. P. Steinberg, and R. R. Chasman, Scission-point model of nuclear-fission based on deformed-shell effects, Phys. Rev. C **14**, 1832 (1976).

[10] G. Scamps and C. Simenel, Impact of pear-shaped fission fragments on mass-asymmetric fission in actinides, Nature (London) **564**, 382 (2018).

[11] G. Scamps and C. Simenel, Effect of shell structure on the fission of sub-lead nuclei, Phys. Rev. C **100**, 041602(R) (2019).

[12] J. P. Unik, L. E. Glendenin, K. F. Flynn, A. Gorski, and R. K. Sjoblom, Fragment mass and kinetic energy distributions for fissioning systems ranging from mass 230 to 256, in *IAEA Third Symposium on Physis and Chemistry of Fission* (IAEA, Vienna, 1974), Vol. II, pp. 19–45

[13] K.-H. Schmidt, S. Steinhäuser, C. Böckstiegel, A. Grewe, A. Heinz, A. R. Junghans, J. Benlliure, H.-G. Clerc, M. de Jong, J. Müller, M. Pfützner, and B. Voss, Relativistic radioactive beams: A new access to nuclear-fission studies, Nucl. Phys. A **665**, 221 (2000).

[14] C. Böckstiegel, S. Steinhäuser, K.-H. Schmidt, H.-G. Clerc, A. Grewe, A. Heinz, M. de Jong, A. R. Junghans, J. Müller, and B. Voss, Nuclear-fission studies with relativistic secondary beams: Analysis of fission channels, Nucl. Phys. A **802**, 12 (2008).

[15] A. Chatillon, J. Taïeb, H. Alvarez-Pol, L. Audouin, Y. Ayyad, G. Bélier, J. Benlliure, G. Boutoux, M. Caamaño, E. Casarejos, D. Cortina-Gil, A. Ebran, F. Farget, B. Fernández-Domínguez, T. Gorbinet, L. Grente, A. Heinz, H. T. Johansson, B. Jurado, A. Kelić-Heil *et al.*, Experimental study of nuclear fission along the thorium isotopic chain: From asymmetric to symmetric fission, Phys. Rev. C **99**, 054628 (2019).

[16] K. Mahata, C. Schmitt, S. Gupta, A. Shrivastava, G. Scamps, and K.-H. Schmidt, Evidence for the general dominance of proton shells in low-energy fission, Phys. Lett. B **825**, 136859 (2022).

[17] C. Schmitt, A. Lemasson, K.-H. Schmidt, A. Jhingan, S. Biswas, Y. H. Kim, D. Ramos, A. N. Andreyev, D. Curien, M. Ciemala, E. Clément, O. Dorvaux, B. De Canditiis, F. Didierjean, G. Duchêne, J. Dudouet, J. Frankland, B. Jacquot, C. Raison, D. Ralet *et al.*, Experimental evidence for common driving effects in low-energy fission from sublead to actinides, Phys. Rev. Lett. **126**, 132502 (2021).

[18] A. Chatillon, J. Taïeb, A. Heinz, H. Alvarez-Pol, L. Audouin, Y. Ayyad, G. Bélier, J. Benlliure, G. Boutoux, M. Caamaño, E. Casarejos, D. Cortina-Gil, A. Ebran, F. Farget, B. Fernández-Domínguez, T. Gorbinet, L. Grente, H. T. Johansson, B. Jurado, A. Kelić-Heil *et al.*, Influence of proton and neutron deformed shells on the asymmetric fission of thorium isotopes, Phys. Rev. C **106**, 024618 (2022).

[19] D. Ramos, M. Caamaño, F. Farget, C. Rodríguez-Tajes, A. Lemasson, C. Schmitt, L. Audouin, J. Benlliure, E. Casarejos, E. Clement, D. Cortina, O. Delaune, X. Derkx, A. Dijon, D. Doré, B. Fernández-Domínguez, G. de France, A. Heinz, B. Jacquot, C. Paradela *et al.*, Experimental evidence of the effect of nuclear shells on fission dissipation and time, Phys. Rev. C **107**, L021601 (2023).

[20] V. M. Strutinsky, Shell effects in nuclear masses and deformation energies, Nucl. Phys. A **95**, 420 (1967).

[21] V. Strutinsky, "Shells" in deformed nuclei, Nucl. Phys. A **122**, 1 (1968).

[22] J. Tōke, R. Bock, G. X. Dai, A. Gobbi, S. Gralla, K. D. Hildenbrand, J. Kuzminski, W. F. J. Müller, A. Olmi, H. Stelzer, B. B. Back, and S. Bjørnholm, Quasi-fission: The mass-drift mode in heavy-ion reactions, Nucl. Phys. A **440**, 327 (1985).

[23] D. J. Hinde, M. Dasgupta, and E. C. Simpson, Experimental studies of the competition between fusion and quasifission in the formation of heavy and superheavy nuclei, Prog. Part. Nucl. Phys. **118**, 103856 (2021).

[24] R. du Rietz, E. Williams, D. J. Hinde, M. Dasgupta, M. Evers, C. J. Lin, D. H. Luong, C. Simenel, and A. Wakhle, Mapping quasifission characteristics and timescales in heavy element formation reactions, Phys. Rev. C **88**, 054618 (2013).

[25] E. Williams, K. Sekizawa, D. J. Hinde, C. Simenel, M. Dasgupta, I. P. Carter, K. J. Cook, D. Y. Jeung, S. D. McNeil, C. S. Palshetkar, D. C. Rafferty, K. Ramachandran, and A. Wakhle, Exploring zeptosecond quantum equilibration dynamics: From deep-inelastic to fusion-fission outcomes in ^{58}Ni + ^{60}Ni reactions, Phys. Rev. Lett. **120**, 022501 (2018).

[26] C. Simenel, K. Godbey, and A. S. Umar, Timescales of quantum equilibration, dissipation and fluctuation in nuclear collisions, Phys. Rev. Lett. **124**, 212504 (2020).

[27] M. G. Itkis, J. Äystö, S. Beghini, A. A. Bogachev, L. Corradi, O. Dorvaux, A. Gadea, G. Giardina, F. Hanappe, I. M. Itkis, M. Jandel, J. Kliman, S. V. Khlebnikov, G. N. Kniajeva, N. A. Kondratiev, E. M. Kozulin, L. Krupa, A. Latina, T. Materna, G. Montagnoli *et al.*, Shell effects in fission and quasi-fission of heavy and superheavy nuclei, Nucl. Phys. A **734**, 136 (2004).

[28] K. Nishio, H. Ikezoe, S. Mitsuoka, I. Nishinaka, Y. Nagame, Y. Watanabe, T. Ohtsuki, K. Hirose, and S. Hofmann, Effects of nuclear orientation on the mass distribution of fission fragments in the reaction of ^{36}S + ^{238}U, Phys. Rev. C **77**, 064607 (2008).

[29] E. M. Kozulin, G. N. Knyazheva, S. N. Dmitriev, I. M. Itkis, M. G. Itkis, T. A. Loktev, K. V. Novikov, A. N. Baranov, W. H. Trzaska, E. Vardaci, S. Heinz, O. Beliuskina, and S. V. Khlebnikov, Shell effects in damped collisions of ^{88}Sr with ^{176}Yb at the Coulomb barrier energy, Phys. Rev. C **89**, 014614 (2014).

[30] A. Wakhle, C. Simenel, D. J. Hinde, M. Dasgupta, M. Evers, D. H. Luong, R. du Rietz, and E. Williams, Interplay between

quantum shells and orientation in quasifission, Phys. Rev. Lett. **113**, 182502 (2014).

[31] M. Morjean, D. J. Hinde, C. Simenel, D. Y. Jeung, M. Airiau, K. J. Cook, M. Dasgupta, A. Drouart, D. Jacquet, S. Kalkal, C. S. Palshetkar, E. Prasad, D. Rafferty, E. C. Simpson, L. Tassan-Got, K. Vo-Phuoc, and E. Williams, Evidence for the role of proton shell closure in quasifission reactions from x-ray fluorescence of mass-identified fragments, Phys. Rev. Lett. **119**, 222502 (2017).

[32] D. J. Hinde, D. Y. Jeung, E. Prasad, A. Wakhle, M. Dasgupta, M. Evers, D. H. Luong, R. du Rietz, C. Simenel, E. C. Simpson, and E. Williams, Sub-barrier quasifission in heavy element formation reactions with deformed actinide target nuclei, Phys. Rev. C **97**, 024616 (2018).

[33] D. Y. Jeung, D. J. Hinde, M. Dasgupta, C. Simenel, E. C. Simpson, K. J. Cook, H. M. Albers, J. Buete, I. P. Carter, C. Düllmann, J. Khuyagbaatar, B. Kindler, N. Lobanov, B. Lommel, C. Mokry, E. Prasad, J. Runke, C. Sengupta, J. F. Smith, P. Thörle-Pospiech *et al.*, Sequential fission and the influence of ^{208}Pb closed shells on the dynamics of superheavy element synthesis reactions, Phys. Lett. B **837**, 137641 (2023).

[34] A. Yu. Chizhov, M. G. Itkis, I. M. Itkis, G. N. Kniajeva, E. M. Kozulin, N. A. Kondratiev, I. V. Pokrovsky, R. N. Sagaidak, V. M. Voskressensky, A. V. Yeremin, L. Corradi, A. Gadea, A. Latina, A. M. Stefanini, S. Szilner, M. Trotta, A. M. Vinodkumar, S. Beghini, G. Montagnoli, F. Scarlassara *et al.*, Unexpected entrance-channel effect in the fission of ^{216}Ra*, Phys. Rev. C **67**, 011603(R) (2003).

[35] D. J. Hinde, R. du Rietz, D. Y. Jeung, K. J. Cook, M. Dasgupta, E. C. Simpson, R. G. Thomas, M. Evers, C. J. Lin, D. H. Luong, L. R. Gasques, R. Rafiei, A. Wakhle, and C. Simenel, Experimental investigation of the role of shell structure in quasifission mass distributions, Phys. Rev. C **106**, 064614 (2022).

[36] G. G. Adamian, N. V. Antonenko, and W. Scheid, Characteristics of quasifission products within the dinuclear system model, Phys. Rev. C **68**, 034601 (2003).

[37] M. Huang, Z. Gan, X. Zhou, J. Li, and W. Scheid, Competing fusion and quasifission reaction mechanisms in the production of superheavy nuclei, Phys. Rev. C **82**, 044614 (2010).

[38] S. Q. Guo, Y. Gao, J. Q. Li, and H. F. Zhang, Dynamical deformation in heavy ion reactions and the characteristics of quasifission products, Phys. Rev. C **96**, 044622 (2017).

[39] V. Zagrebaev and W. Greiner, Unified consideration of deep inelastic, quasi-fission and fusion-fission phenomena, J. Phys. G: Nucl. Part. Phys. **31**, 825 (2005).

[40] Y. Aritomo, K. Hagino, K. Nishio, and S. Chiba, Dynamical approach to heavy-ion induced fission using actinide target nuclei at energies around the Coulomb barrier, Phys. Rev. C **85**, 044614 (2012).

[41] A. V. Karpov and V. V. Saiko, Modeling near-barrier collisions of heavy ions based on a Langevin-type approach, Phys. Rev. C **96**, 024618 (2017).

[42] N. Wang, K. Zhao, and Z. Li, Fusion and quasi-fission dynamics in nearly-symmetric reactions, Sci. China Phys. Mech. Astron. **58**, 112001 (2015).

[43] N. Wang and L. Guo, New neutron-rich isotope production in ^{154}Sm + ^{160}Gd, Phys. Lett. B **760**, 236 (2016).

[44] J. Klimo, M. Veselsky, G. Souliotis, and A. Bonasera, Simulation of fusion and quasi-fission in nuclear reactions leading to production of superheavy elements using the constrained molecular dynamics model, Nucl. Phys. A **992**, 121640 (2019).

[45] C. Li, J. Tian, and F. Zhang, Production mechanism of the neutron-rich nuclei in multinucleon transfer reactions: A reaction time scale analysis in energy dissipation process, Phys. Lett. B, **809** 135697 (2020).

[46] Y. Feng, Y. Huang, E. Xiao, X. Lei, L. Zhu, and J. Su, Contributions of quasifission and fusion-fission in the ^{24}Mg + ^{178}Hf reaction at 145 MeV laboratory beam energy using the Boltzmann-Uehling-Uhlenbeck model, Phys. Rev. C **107**, 044606 (2023).

[47] V. E. Oberacker, A. S. Umar, and C. Simenel, Dissipative dynamics in quasifission, Phys. Rev. C **90**, 054605 (2014).

[48] K. Hammerton, Z. Kohley, D. J. Hinde, M. Dasgupta, A. Wakhle, E. Williams, V. E. Oberacker, A. S. Umar, I. P. Carter, K. J. Cook, J. Greene, D. Y. Jeung, D. H. Luong, S. D. McNeil, C. S. Palshetkar, D. C. Rafferty, C. Simenel, and K. Stiefel, Reduced quasifission competition in fusion reactions forming neutron-rich heavy elements, Phys. Rev. C **91**, 041602(R) (2015).

[49] A. S. Umar, V. E. Oberacker, and C. Simenel, Shape evolution and collective dynamics of quasifission in the time-dependent Hartree-Fock approach, Phys. Rev. C **92**, 024621 (2015).

[50] A. S. Umar, V. E. Oberacker, and C. Simenel, Fusion and quasifission dynamics in the reactions ^{48}Ca + ^{249}Bk and ^{50}Ti + ^{249}Bk using a time-dependent Hartree-Fock approach, Phys. Rev. C **94**, 024605 (2016).

[51] K. Sekizawa and K. Yabana, Time-dependent Hartree-Fock calculations for multinucleon transfer and quasifission processes in the ^{64}Ni + ^{238}U reaction, Phys. Rev. C **93**, 054616 (2016).

[52] Y. Chong and G. Lu, Angular momentum dependence of quasifission dynamics in the reaction ^{48}Ca + ^{244}Pu, Sci. China Phys. Mech. Astron. **60**, 092011 (2017).

[53] S. Ayik, B. Yilmaz, O. Yilmaz, and A. S. Umar, Quantal diffusion description of multinucleon transfers in heavy-ion collisions, Phys. Rev. C **97**, 054618 (2018).

[54] K. Godbey, A. S. Umar, and C. Simenel, Deformed shell effects in ^{48}Ca + ^{249}Bk quasifission fragments, Phys. Rev. C **100**, 024610 (2019).

[55] C. Simenel, P. McGlynn, A. S. Umar, and K. Godbey, Comparison of fission and quasi-fission modes, Phys. Lett. B **822**, 136648 (2021).

[56] L. Li, L. Guo, K. Godbey, and A. S. Umar, Impact of tensor force on quantum shell effects in quasifission reactions, Phys. Lett. B **833**, 137349 (2022).

[57] P. McGlynn and C. Simenel, Time-dependent Hartree-Fock study of quasifission trajectories in reactions forming ^{294}Og, Phys. Rev. C **107**, 054614 (2023).

[58] C. Simenel, Nuclear quantum many-body dynamics, Eur. Phys. J. A **48**, 152 (2012).

[59] C. Simenel and A. S. Umar, Heavy-ion collisions and fission dynamics with the time-dependent Hartree-Fock theory and its extensions, Prog. Part. Nucl. Phys. **103**, 19 (2018).

[60] K. Sekizawa, TDHF theory and its extensions for the multinucleon transfer reaction: A mini review, Front. Phys. **7**, 20 (2019).

[61] P. D. Stevenson and M. C. Barton, Low–energy heavy-ion reactions and the Skyrme effective interaction, Prog. Part. Nucl. Phys. **104**, 142 (2019).

[62] K. Godbey and A. S. Umar, Quasifission dynamics in microscopic theories, Front. Phys. **8**, 40 (2020).

[63] K.-H. Kim, T. Otsuka, and P. Bonche, Three-dimensional TDHF calculations for reactions of unstable nuclei, J. Phys. G: Nucl. Part. Phys. **23**, 1267 (1997).
[64] P.-G. Reinhard, B. Schuetrumpf, and J. A. Maruhn, The axial Hartree-Fock + BCS code SkyAx, Comput. Phys. Commun. **258**, 107603 (2021).
[65] S. Ebata and T. Nakatsukasa, Pairing effects in nuclear fusion reaction, JPS Conf. Proc. **1**, 013038 (2014).
[66] Y. Hashimoto and G. Scamps, Gauge angle dependence in time-dependent Hartree-Fock-Bogoliubov calculations of $^{20}O + ^{20}O$ head-on collisions with the Gogny interaction, Phys. Rev. C **94**, 014610 (2016).
[67] P. Magierski, K. Sekizawa, and G. Wlazłowski, Novel role of superfluidity in low–energy nuclear reactions, Phys. Rev. Lett. **119**, 042501 (2017).
[68] J. A. Maruhn, P.-G. Reinhard, P. D. Stevenson, and A. S. Umar, The TDHF code Sky3D, Comput. Phys. Commun. **185**, 2195 (2014).
[69] B. Schuetrumpf, P.-G. Reinhard, P. D. Stevenson, A. S. Umar, and J. A. Maruhn, The TDHF code Sky3D version 1.1, Comput. Phys. Commun. **229**, 211 (2018).
[70] W. J. Świątecki, K. Siwek-Wilczyńska, and J. Wilczyński, Fusion by diffusion. II. Synthesis of transfermium elements in cold fusion reactions, Phys. Rev. C **71**, 014602 (2005).
[71] A. Jedele, A. B. McIntosh, K. Hagel, M. Huang, L. Heilborn, Z. Kohley, L. W. May, E. McCleskey, M. Youngs, A. Zarrella, and S. J. Yennello, Characterizing neutron-proton equilibration in nuclear reactions with subzeptosecond resolution, Phys. Rev. Lett. **118**, 062501 (2017).
[72] A. S. Umar, C. Simenel, and W. Ye, Transport properties of isospin asymmetric nuclear matter using the time-dependent Hartree-Fock method, Phys. Rev. C **96**, 024625 (2017).
[73] V. I. Zagrebaev, Yu. Ts. Oganessian, M. G. Itkis, and W. Greiner, Superheavy nuclei and quasi-atoms produced in collisions of transuranium ions, Phys. Rev. C **73**, 031602(R) (2006).
[74] D. J. Kedziora and C. Simenel, New inverse quasifission mechanism to produce neutron-rich transfermium nuclei, Phys. Rev. C **81**, 044613 (2010).
[75] E. M. Kozulin, V. I. Zagrebaev, G. N. Knyazheva, I. M. Itkis, K. V. Novikov, M. G. Itkis, S. N. Dmitriev, I. M. Harca, A. E. Bondarchenko, A. V. Karpov, V. V. Saiko, and E. Vardaci, Inverse quasifission in the reactions $^{156,160}Gd + ^{186}W$, Phys. Rev. C **96**, 064621 (2017).
[76] V. E. Viola, K. Kwiatkowski, and M. Walker, Systematics of fission fragment total kinetic-energy release, Phys. Rev. C **31**, 1550 (1985).
[77] D. J. Hinde, J. R. Leigh, J. J. M. Bokhorst, J. O. Newton, R. L. Walsh, and J. W. Boldeman, Mass-split dependence of the pre- and post-scission neutron multiplicities for fission of ^{251}Es, Nucl. Phys. A **472**, 318 (1987).
[78] M. Wang, W. Huang, F. Kondev, G. Audi, and S. Naimi, The AME 2020 atomic mass evaluation (II). Tables, graphs and references, Chin. Phys. C **45**, 030003 (2021).